Coherent Fourier scatterometry using rotational scanning

Soman, Sarika; In 't Velt, Bastiaan; Horsten, Roland; Pereira, Silvania

DOI
10.1117/1.OE.64.7.074106

Publication date
2025

Document Version
Final published version

Published in
Optical Engineering

OE Optical Engineering

RESEARCH PAPER

Coherent Fourier scatterometry using rotational scanning

Sarika Soman,* Bastiaan In 't Velt, Roland Horsten, and Silvania Pereira
Delft University of Technology, Department of Imaging Physics, Delft, The Netherlands

ABSTRACT. We present a rotation-based coherent Fourier scatterometry (CFS) system for high-speed, high-resolution surface metrology. Traditional CFS systems rely on piezoelectric stages for point-by-point raster scanning, which limits scan speed due to constant accelerations and decelerations. In our approach, the fast-axis piezo stage is replaced by a rotation stage moving at constant angular velocity, whereas the slow-axis piezo is used to step radially outward to generate concentric scan paths. We introduce a frequency spread–based technique to compensate for probe centering deviation and demonstrate the capability of measuring axial wobble using depth-sensitive CFS signals. Application of the system is shown through the detection of 0.4 μm polystyrene latex particles and the calibration of etched pits with diameters ranging from 225 to 1125 nm at the wavelength of 633 nm. The proposed system offers a scalable and low-complexity solution for fast, noncontact nanometrology.

Keywords: metrology; scatterometry; optical metrology; coherent Fourier scatterometry; high-speed; rotation

Paper 20250313G received Apr. 17, 2025; revised Jun. 24, 2025; accepted Jun. 25, 2025; published Jul. 17, 2025.

1 Introduction

Fast, accurate, and robust metrology tools are critical in modern manufacturing environments for enabling real-time process monitoring and reducing production bottlenecks.[1–4] Traditional high-resolution tools, such as scanning electron microscopy and atomic force microscopy, are limited by slow scan speeds, destructive testing, and strict operational requirements.[5,6] Optical techniques such as scatterometry overcome these limitations by offering rapid, noncontact measurement capabilities.[7–9]

Scatterometry refers to a broad category of model-based optical metrology methods[10–13] that work by directing light beams at various angles or wavelengths onto a sample and analyzing changes in polarization or intensity in the far field. Coherent Fourier scatterometry (CFS) is an advanced scatterometry technique in which the scattering response of multiple plane waves from different angles is measured simultaneously.[14] This technique has been successfully applied to a wide range of applications, including diffraction grating characterization,[15] nerve crossing detection,[16] defect detection on SiC layer for power electronics,[17] and nanoparticle characterization on Si wafers and plastic substrates.[18] CFS uses a focused spot, generated using an objective, as a probe to scan the sample surface. The light after reflection from the sample is collected by the same objective. The reflected field is measured using a detector placed in the Fourier plane, i.e., the back focal plane of the objective. The field recorded in the Fourier plane for each scan position is stitched together to create a scattering map of the sample surface.

*Address all correspondence to Sarika Soman, s.soman@tudelft.nl

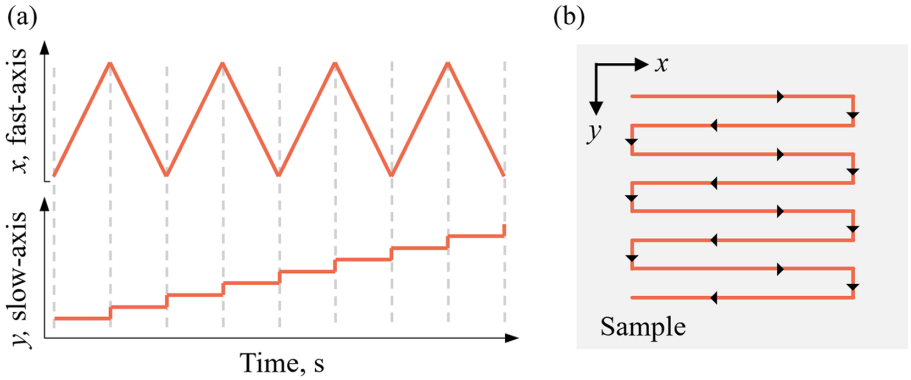

Fig. 1 Schematic of raster scanning. (a) Input waveforms used to drive the piezo stages along the fast (x) and slow (y) axes. (b) The raster pattern traced on the sample surface.

Owing to its small spot size, the use of a focused spot as a probe enables high spatial resolution. However, additional scanning mechanisms are therefore required to scan a complete sample surface. In conventional CFS setups, the sample is scanned laterally using 2D piezo stages. However, it comes at the cost of long scan times for large scan areas, posing a significant limitation for many industrial applications. To address this drawback, we previously proposed a scanning strategy using parallel probes to reduce the scan time for a given scan area.[19] The scan time reduces with the number of probes, but the drawback is that each probe requires its own detector and acquisition channels. This can increase the electronic complexity as the number of probes increases. Another strategy would be to use a different kind of mechanical scanning. In this work, this approach is implemented using a rotation-based scanning.

Raster scanning traditionally employs two piezo stages: one along the fast axis and another along the slow axis to create a 2D map. Figure 1 shows the input waveforms applied to the two stages and the corresponding raster pattern traced on the sample surface. The piezo stage along the fast axis, following a triangular waveform, must accelerate, decelerate, and reverse the motion for each line, whereas the slow-axis stage moves incrementally following a staircase or slow ramp signal.[20] This repeated start–stop motion limits scan speed and throughput. Each reversal requires settling time, slowing the process for large-area scans.[20] High speeds can also excite mechanical resonance in the system, causing vibrations that reduce positional accuracy.[21] To avoid this, systems must operate below resonance limits, further reducing speed.

Rotational scanning avoids these problems using a rotation stage that moves at constant angular velocity.[22–25] This eliminates start–stop motion and keeps vibrations low. In the proposed solution, the fast-axis motion is replaced by the rotation stage, whereas the slow axis is handled by a piezo stage stepping outward in concentric circles. The result is smoother motion, higher scan speeds, and better throughput. In addition, it is cost-effective and simplifies the control system while being able to scan large areas with high resolution. In this setup, we use a staircase waveform for the slow-axis motion, leading to a concentric circle scan pattern. Using a slow ramp signal instead generates a spiral scan pattern.

Despite its advantages, rotational scanning presents new challenges. One of the primary concerns is the centering deviation of the probe.[26–29] When the probe, i.e., the focused spot, is misaligned with respect to the rotational axis of the stage, it introduces distortions in the reconstructed scan. To address this, we propose a simple and general solution to minimize this deviation without requiring additional sensors or calibrated targets. The method uses the spread in the frequency spectrum of the scan signal at different radial distances to minimize the centering error.

Nonuniform sampling is another potential challenge. Scanning speed increases as a linear function of the scan radius. This means that, at constant sampling frequency, as the scan radius increases, the sampling becomes increasingly sparse and can also influence the measurement accuracy. Possible solutions are either to vary the angular velocity of the rotation stage inversely with the scan radius or to adaptively increase the sampling rate. For the limited scanning range in our setup, neither option was considered to be necessary, and both the sampling rate and the angular velocity were kept fixed. However, for larger radial distances, different solutions should be implemented.

Finally, the error motion of the rotation stage can also introduce challenges. The axial and radial runout errors of the rotation stage can distort the sample scan signal.[30–32] Depending on the mechanical precision of the rotating stage, additional servos might be required to track focusing and tracking errors.[33] This was not considered necessary for the rotation stage used in our setup. Nonetheless, we detail a method to estimate the axial wobble of the system using the CFS scan signal.

The remainder of the paper is organized as follows: Section 2 covers the theoretical foundation, Sec. 3 describes the experimental setup, Sec. 4 discusses reconstruction methods and probe offset correction, Sec. 5 presents axial wobble measurement, Sec. 6 shows practical applications, and Sec. 7 summarizes conclusions and future directions.

2 Measurement Principle

CFS is a model-based optical metrology tool used for precise nanostructure characterization. It uses an objective lens to transform a collimated beam into a focused spot on the sample, where each point in the back focal plane of the objective corresponds to a distinct angle of incidence. The scattered field reflected from the sample is captured by the same objective lens, and the field at the Fourier plane (corresponding to the back focal plane of the objective) is recorded using a camera or split detector for further analysis.[14]

The split detector consists of a bi-cell with two photodiodes (**L** and **R**) positioned side by side. It is placed at the Fourier plane and positioned to ensure that the scattered field is incident at the midpoint between the two photodiodes. Each diode integrates the field it receives, and the difference signal, $\mathbf{L} - \mathbf{R}$, is recorded. The bi-cell is oriented such that the two photo diodes lie on a line parallel to the direction of the scan.

When the scattered field is symmetric, the difference signal is 0. As the focused spot is scanned across the sample, asymmetries in the scattered field produce a nonzero difference signal. Figure 2 illustrates a simulated scan signal of a focused spot (linearly polarized at the Fourier

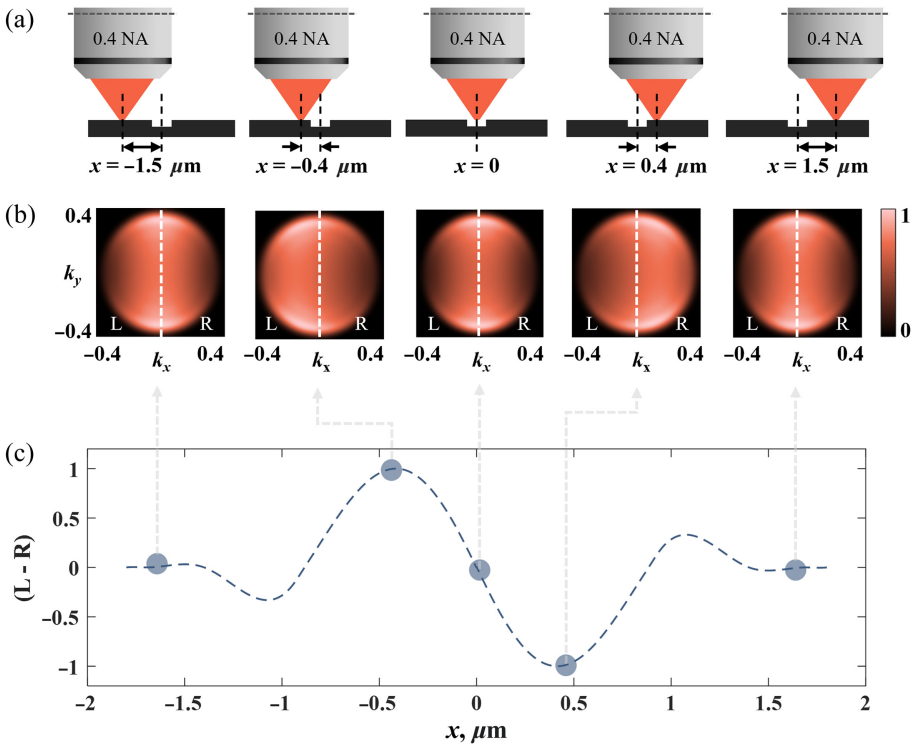

Fig. 2 Simulation of the CFS in the Fourier plane signal using a 0.4 NA focused spot with 633 nm wavelength to scan a pit of 400 nm diameter and 150 nm depth etched into Si. (a) The position of the focused spot with respect to the etched pit and (b) corresponding intensity of reflected field in the Fourier plane, for points on the (c) difference signal shown in dashed lines. The difference signal is generated from multiple simulations with different positions of the spot with respect to the etched pit. The polarization at the objective is linear, along the *x*-axis.

plane in the x-direction, 0.4 NA, 633 nm wavelength) scanning across a circular pit with a 400 nm diameter and 150 nm depth. The field intensity at the Fourier plane is shown for various spot positions. Details of the simulations are provided in Appendix A.

3 Experimental Setup

The experimental setup is shown in Fig. 3. The CFS scan head consists of the following: Laser (FP-D-635-1P-C-C, Laser Components, Olching, Germany) generating 1 mW, 635 nm wavelength collimated light, Lens L1, an aspheric lens of 0.65 NA with focal length of 2 mm and lens L2 with focal length of 25 mm; beam splitters BS1 and BS2; split detector SD, consisting of a bi-cell (SD 113-24-21-021) for generating the difference signal; and CCD camera for localizing areas of interest. The collimated light from the laser is focused on the sample using L1. The scattered light after reflection is captured using the same lens. L2 images the Fourier plane or the back focal plane of lens L1 onto the detector. BS2 splits the reflected light onto a camera and a split detector.

The entire setup is enclosed in a custom-made, 3D printed housing and mounted on a piezo $x-y-z$ translator (P-611.3S NanoCube, Physik Instrumente, Karlsruhe, Germany) for slow-axis movements and focus positioning. There are additional manual translators for coarse adjustments. The rotating stage (Precilec 36SMOP-17, VDL ETG, Eindhoven, The Netherlands) is a DC torque motor controlled using an external voltage supply.

3.1 Scanning and Synchronization

The sample is scanned using a combination of the rotation stage and the x or y piezo translator. The sample is mounted on the rotation stage, which rotates continuously at a frequency of

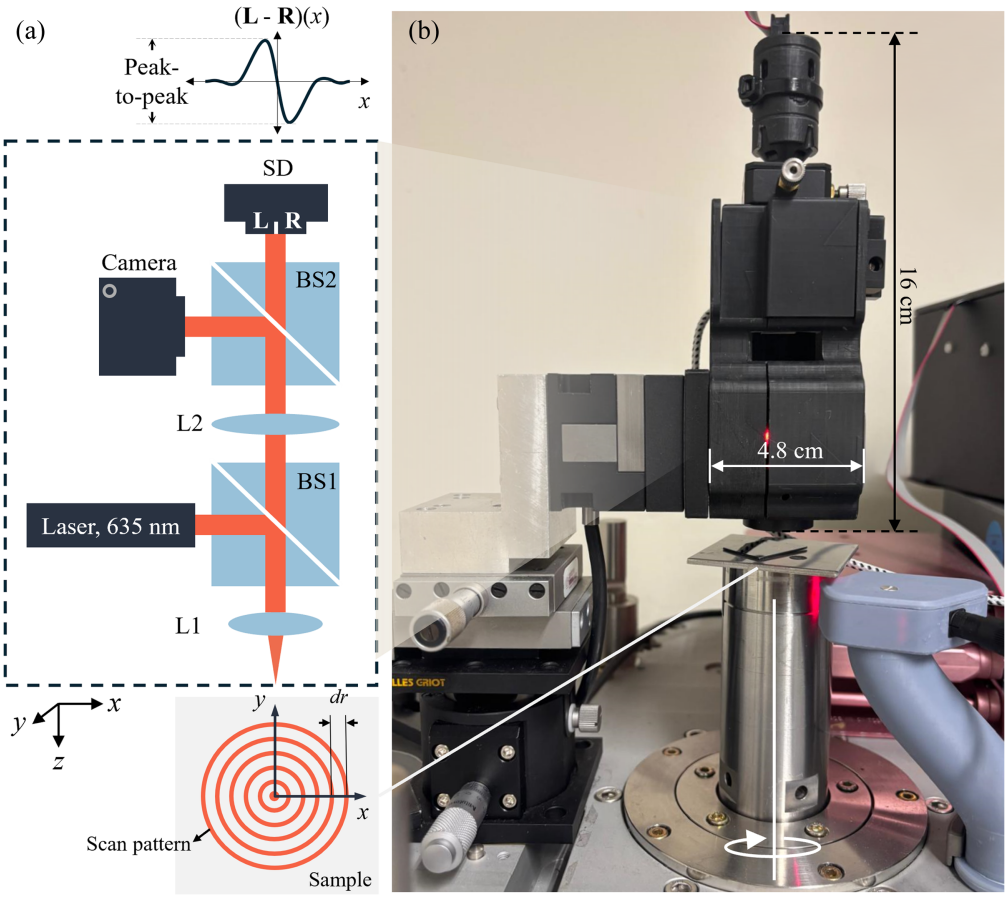

Fig. 3 (a) Schematic of the CFS setup used for scanning with L1 and L2—lenses with 2 and 25 mm focal lengths, respectively; BS1, BS2—beam splitters; SD—split detector, 635 nm laser; and a camera to localize areas of interest on the sample. (b) Photo of the setup on the optical table.

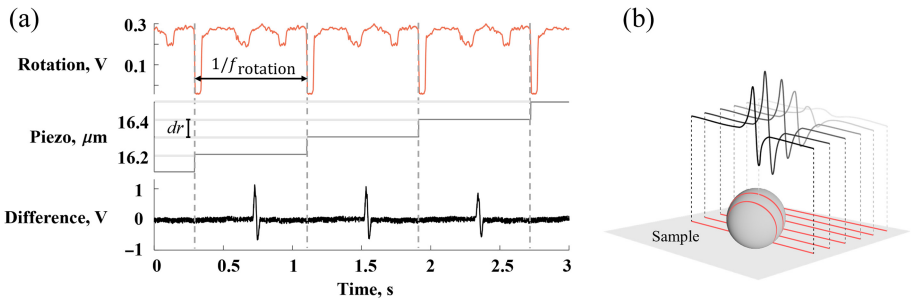

Fig. 4 (a) Data recorded from multiple channels during a typical sample scan: rotation—data from the rotation sensor with the dips denoting the completion of one rotation, piezo—feedback signal from the in-built position sensor, difference—difference signal generated using the split detector. Dotted lines are used to denote different rotations. The scan parameters are as follows: $f_{\text{rotation}} = 1.23$ Hz, $dr = 0.1$ μm. The sample consists of a Si wafer with 1 μm PSL particles. (b) Schematic of the scanning process over a particle: red lines indicate scan paths; black traces show corresponding difference signals.

f_{rotation}. The CFS scan head is moved radially using the piezo translator. The resulting scan pattern consists of concentric circles with increasing radii. The piezo stage steps by a predefined amount, $dr <$ spot size, as the rotation stage completes one rotation or after every $1/f_{\text{rotation}}$ second.

Due to the absence of a rotation stage encoder, a simplified rotation counter was built to synchronize the piezo stage with the rotation cycles. The rotation sensor consists of a laser, a photo diode, and a scattering object fixed on the rotating cylinder. As the scattering object passes through the laser beam, it reduces the reflected light received by the photo diode, creating dips in the recorded signal. These dips are used as markers to count rotation. Figure 4(a) shows an example of the rotation sensor, piezo (x-axis), and difference signals acquired during a sample scan [1 μm polystyrene latex (PSL) particle on Si]. The dips from the rotation sensor are used to trigger the piezo to step in the radial direction, whereas the difference signal is acquired continuously. The split detector, rotation sensor, and piezo feedback data are digitized by a data acquisition card (NI 9222, National Instruments, Austin, Texas) and recorded by the computer.

Figure 4(b) shows a schematic of the signal generation during the scanning of a particle on a flat substrate. The red lines follow the scan lines across the sample surface. The difference signal plotted in black illustrates the variation in peak-to-peak amplitude of the difference signal as a function of the offset between the particle center and the scan line. A similar trend can also be seen in the example difference signal, as shown in Fig. 4(a).

4 Surface Topography Reconstruction

Feedback signals, generated by the rotation sensor and piezo stage, provide real-time positional data that correlate the scanned signal to specific sample locations. The information on the radial coordinate is given by the piezo feedback, and the azimuthal position is calculated from the rotation counter sensor. Assuming uniform sampling, the azimuthal position of i'th data sample is $2\pi i/N$, where N is the total number of samples per rotation. Figure 5(a) shows the polar 2D representation of the scan signal. The sample is a three-line Si grating. Polar to Cartesian coordinate transformations follows the simple relation

$$x_i = r_i \cos \theta_i, \tag{1}$$

$$y_i = r_i \sin \theta_i, \tag{2}$$

where r_i and θ_i refer to the radial and azimuthal coordinates of the i'th data sample and x_i y_i refer to the corresponding Cartesian coordinates. Figure 5(b) shows the 2D reconstruction in Cartesian coordinates.

We now consider some nuances involved in the 2D reconstruction process. The first is the variation in rotation speed. In an ideal system, the rotational speed remains constant over time. However, in practice, the speed tends to drift due to the mechanical properties of the rotation

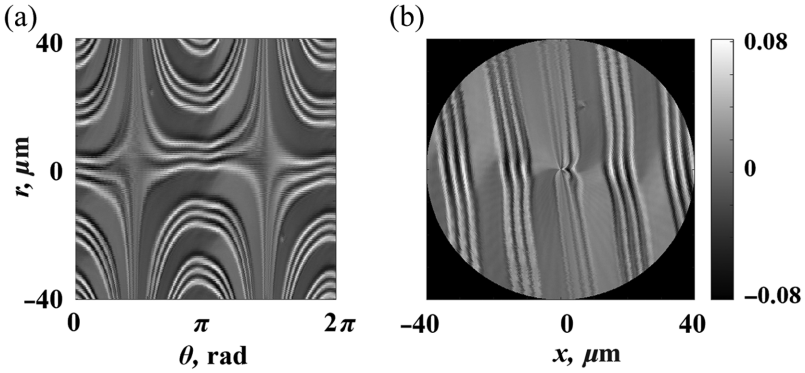

Fig. 5 2D reconstruction of the scan sample surface: (a) polar representation and (b) Cartesian representation. The probe is a 0.65 NA focused spot with a 635 nm wavelength. The sample consists of a three-line Si grating scanned with $f_{\text{rotation}} = 1.64$ Hz and radial step size, $dr = 0.1$ μm.

stage. As a result, the number of data points per rotation, N, is not uniform across different rotations. To ensure accurate 2D reconstruction, the acquired data points must first be resampled so that each rotation contains the same number of data points. For the data shown in Fig. 5, the data points are first resampled using linear interpolation before the 2D reconstruction.

The second issue is that of the probe centering deviation. During the scan, the CFS scan head, which is mounted on the piezo stage, steps along the radial direction, whereas the sample mounted on the rotation stage is rotated continuously. The intention is, of course, that the piezo movement starts from the center of rotation or the rotation axis and then steps outward. However, the piezo and the rotation stages are independent systems, and their movements are not coupled. It is therefore hard to determine the position of the rotation axis with the accuracy required for nanostructure measurements. The result is that the beginning of the piezo movement may not coincide with the rotation axis. The influence of the piezo offset on the 2D reconstruction, as well as the proposed solution to minimize this offset, is detailed in Secs. 4.1 and 4.2.

4.1 Probe Centering Deviations

For accurate 2D reconstruction, it is assumed that the center of rotation coincides with the starting point of the piezo scan range. However, if there is an unknown offset between these two, the reconstructed data may exhibit distortions that vary based on both the magnitude and direction of the offset. Figure 6 shows a schematic of the spot offset with respect to the rotation axis. The figure shows a general case with nonzero offsets along both the x- and y-directions. To quantify the impact of the offset on the reconstruction, we derive the mathematical correction required to align the data properly. Let the true offset of the probe relative to the rotation axis be $(\Delta x, \Delta y)$ (see Fig. 6). The uncorrected polar coordinates of a data point are (r_i, θ_i), whereas the corrected coordinates are (r_i', θ_i'). The polar coordinates after correcting for the offset are[23]

$$r_i' = \sqrt{(r_i + \Delta x)^2 + (\Delta y)^2}, \quad \theta_i' = \theta_i - \arctan \frac{\Delta y}{r_i + \Delta x} \tag{3}$$

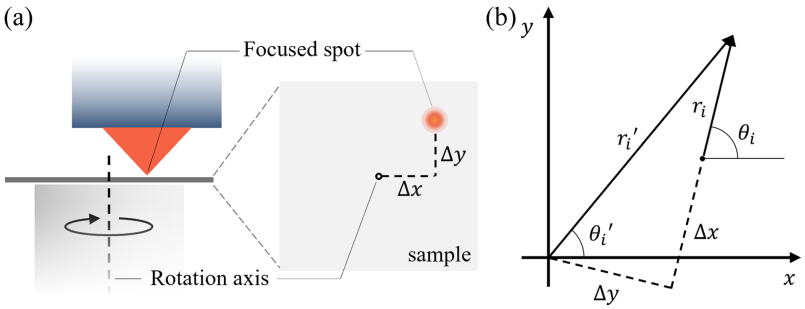

Fig. 6 (a) Schematic of the probe centering offset with respect to rotation axis and (b) polar coordinate of the i'th data point in the polar coordinate system with and without offset correction.

The offset causes nonlinear distortions in the reconstructed data. These distortions are most pronounced at small values of r_i (near the center of the scan) and gradually diminish as r_i becomes significantly larger than the offset ($r_i \gg \Delta x, \Delta y$). As a result, the central region of the scan area is the most affected. This is evident in the scan example, as shown in Fig. 5. The grating lines are no longer straight but are distorted, especially in the center. The centering deviation introduces two major issues. First, the system fails to capture any information within a circular region of radius $\sqrt{\Delta x^2 + \Delta y^2}$ around the true rotation center, leading to a missing data region in the reconstruction. Second, the reconstructed data no longer accurately represent the sample surface topography. The impact of these distortions depends on the specific application. For example, in contamination detection, ensuring that all particles are detected is more critical than achieving a perfectly accurate sample topography. By contrast, applications requiring precise surface profiling, such as semiconductor metrology, demand minimal distortions.

4.2 Minimizing Probe Centering Deviation

To minimize the probe offset, we first need to determine the position of the rotation axis relative to the piezo stage scan. We propose a frequency spread minimization method to achieve this accurately. The scanning process can be approximated as a convolution of the focused spot with the sample surface. In the spatial frequency domain, the frequency content of the scan signal is given by

$$F_{\text{scan signal}} = F_{\text{spot}} \cdot F_{\text{sample}} \tag{4}$$

where F_{spot} and F_{sample} are the spatial frequency spectra of the focused spot and sample, respectively. As, during scanning, we record variations in intensity on the detector as a function of time, the spatial frequency spectrum must be converted into its temporal counterpart. This is achieved by scaling the spatial frequency spectrum by the scan speed, v

$$F^t_{\text{scan signal}} = F_{\text{scan signal}} \cdot v. \tag{5}$$

A simulated example is shown in Fig. 7. The figure shows the scan signals (in blue and orange) from the same sample when scanned at two different scan speeds (v and $3v$). When the scan speed is tripled, the width of the scan signal in the time domain is reduced to a third, whereas the width of the spectrum in the frequency domain is tripled.

For a rotating stage moving at a constant angular velocity ω, the speed, v, with which the focused spot scans the sample is a function of the distance r between the focused spot and the rotation axis: $v = \omega \cdot r$. The frequency spread of the scan signal is thus a linear function of r. We use this frequency spread variation to determine the exact position of the rotation axis in piezo coordinates.

To quantify the variation in frequency spread with the piezo position, we define the following metric:

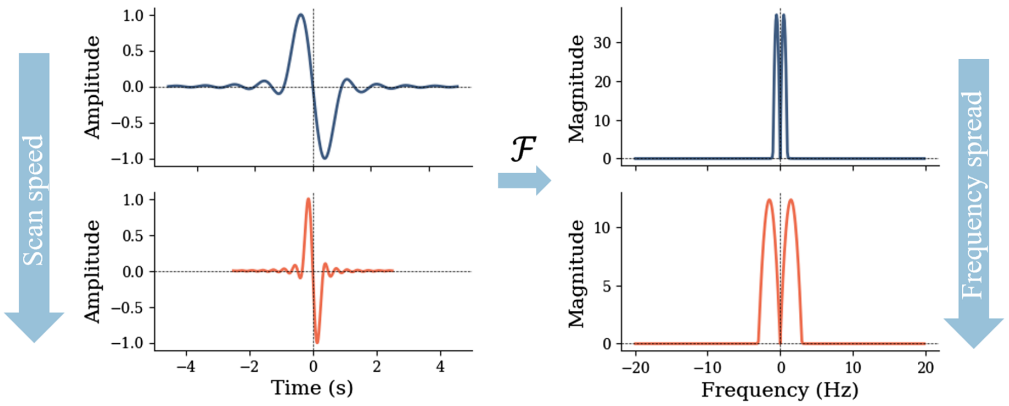

Fig. 7 Schematic illustrating the influence of the scan speed on the signal width in the time domain and the spread in the frequency domain. The blue and orange signals, on the left, correspond to the simulated signal scanned with scan speeds v and $3v$, respectively. The plots on the right show their corresponding frequency spectrum, after the Fourier transformation.

$$S(x) = \sum_{f_i > n f_{\text{rotation}}} |F^t_{\text{scan signal}}(f_i)|^2, \quad \text{with } F^t_{\text{scan signal}} = \mathcal{F}\{d(x)\}, \tag{6}$$

where x is the piezo position, $d(x)$ is the difference signal recorded during one full rotation of the sample, and $f_{\text{rotation}} = \omega/2\pi$ is the fundamental rotation frequency. The parameter n is an integer > 1 that helps to filter out low-frequency components.

The piezo position where $S(x)$ reaches its minimum corresponds to the point closest to the rotation axis

$$x_{\text{rotation axis}} = \underset{x}{\text{argmin}}\, S(x). \tag{7}$$

Figure 8 shows the variation of $S(x)$ as a function of the piezo position along the x- and y-directions. A value of $n = 5$ is used for the calculation of $S(x)$ (see Appendix B). The minima, marked by dotted lines, indicate the coordinates of the rotation axis. For this scan, we determine an offset of 23.0 μm along the x-direction and 17.9 μm along the y-direction. The sample consists of a three-line Si grating fabricated on a Si wafer.

After the offset is calculated, the coordinates assigned to the data points can be corrected using Eq. (3). Figure 9 shows the 2D reconstruction of the scan signal before and after correcting for the probe offset. The figure shows a clear reduction in the distortion near the center of the scan. The remaining distortion could possibly be due to the radial wobble intrinsic to the rotation stage, which is not recorded during the scan.

The advantage of using the frequency spread minimization method to minimize the probe offset is that it does not require any prior knowledge about the geometric dimensions of the sample features or any special components such as wedges.[23,27] However, it does require a

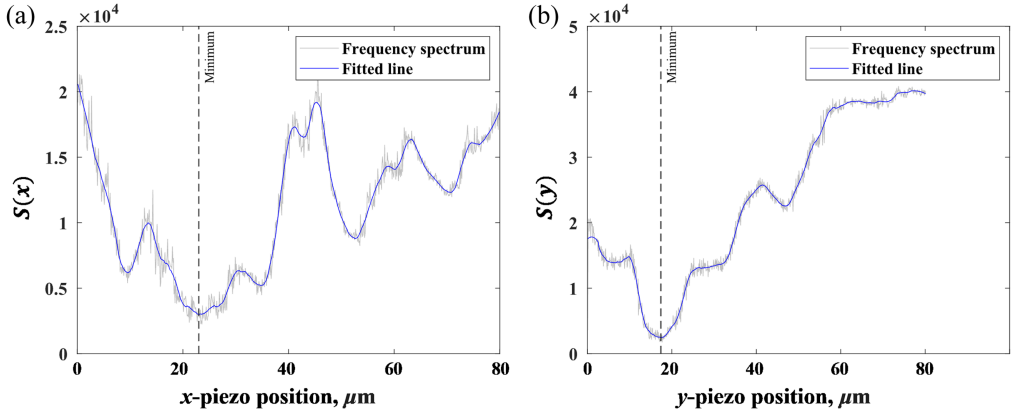

Fig. 8 Frequency spread as a function of the piezo position along (a) x-direction and (b) y-direction. The dotted lines correspond to the coordinates of the rotation axis.

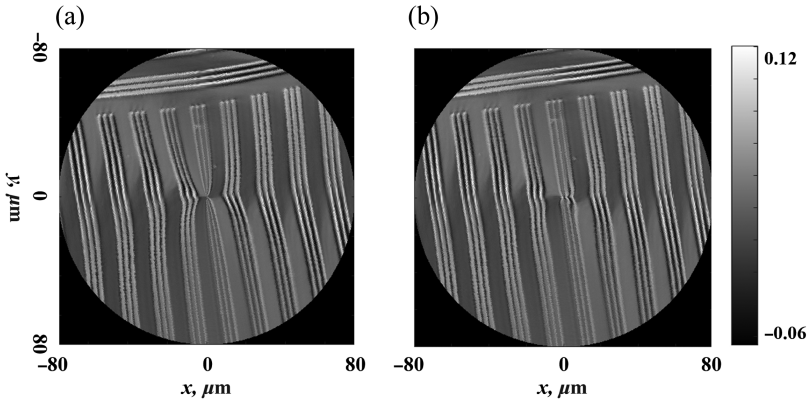

Fig. 9 Scan surface reconstruction (a) before and (b) after offset correction. The offset correction is 23.0 μm along the x-direction and 17.9 μm along the y-direction. The sample consists of a three-line grating scanned with $f_{\text{rotation}} = 1.1$ Hz and $dr = 0.1$ μm.

sample with structures in the scan area and a detector with sufficient bandwidth to capture all the high-frequency signals generated during the scanning process.

A rotation stage exhibits both axial and radial runout errors during its motion. Radial runout refers to deviations perpendicular to the axis of rotation, whereas axial runout involves tilting of the rotation axis relative to its ideal alignment. The influence of radial error is evident in the residual distortion observed near the scan center after offset correction. Although the exact magnitude of the radial error is not quantified here, the frequency spread minimization method could be adapted to enable more precise calculations.

So far, we have focused on minimizing probe offset by analyzing the frequency spectrum of the scan signal. However, axial wobble, defined as displacement along the height direction during rotation, remains another critical source of error. In Sec. 5, we address axial wobble by examining the amplitude variations of the scan signal in the time domain, providing a complementary approach to improve rotational accuracy.

5 Axial Wobble Measurement

In this section, we use the depth response of the CFS scan signal to measure the axial wobble of the rotation stage. The difference signal in a CFS scan varies depending on the measurement plane relative to the focused spot. As the spot has an intensity distribution that changes along the axial direction, its interaction with the sample at different depths alters the scan signal. By analyzing these variations, we can generate a depth response curve that maps the signal changes to axial position. Using the depth response curve, a signal measured at an unknown axial distance can be used to estimate the axial position of the sample. When measuring the sample position mounted on a rotation stage, the scan signal can serve as a proxy for the axial movements of the stage. Two kinds of axial wobble measurements can be made using CFS signals:

1. Height variations along one rotation: The axial position of the stage changes as it rotates. This variation depends on the mechanical properties of the rotation stage.
2. Height variations at a single point across multiple rotations: The axial position is measured at a fixed point during multiple rotations. This can give a measure of repeatability.

Both types of axial wobble can be measured using the CFS scan signal. As the measurement is based on the variation in scan signal as a function of axial position, it is important to have multiple identical structures along one rotation to measure the axial wobble along one rotation. No such requirement is necessary to measure wobble at a specific position. For simplicity, we measure only the axial movement of the stage at a single position across multiple rotations in this study. For both, it is recommended to use a sample with extended structures, such as lines or gratings, to eliminate the influence of radial wobble as radial wobble can shift the position of the spot relative to the scanning structure. If the structure is smaller than the combined size of the spot and wobble, it can also cause variations in the amplitude of the scan signal.

5.1 Creating a Depth–Response Curve

The first step in measuring axial wobble is to create a depth response curve using a sample with extended structures. As the goal is to measure the axial wobble of the rotation stage, we cannot use the same stage to create the curve. Instead, we use the piezo stages along the x, y, and z axes to create a 3D stack of CFS scan signals. Piezo stages allow the sample to be scanned independently with sub-nanometer accuracy. Once the scan signal is obtained, the signal can be quantified by calculating the peak-to-peak value of the difference signal. The variation of this peak-to-peak value is then plotted as a function of the z-axis (axial position).

Figure 10(a) presents the normalized peak-to-peak signal as a function of the axial position. The sample consisted of a Si wafer with 10 μm wide grating lines. The curve is asymmetric about the peak possibly due to asymmetric optical aberrations. The left and right slopes of the curve are linear and can be used as calibration curves. The right slope is chosen as it provides a steeper, more sensitive calibration curve. The slope is calculated to be -0.149 ± 0.010 V/μm with a confidence interval (CI) of 95%. This relation is further used to measure the axial wobble of the stage. The slope is independent of the sample properties and depends only on the optical characteristics of the focused spot.

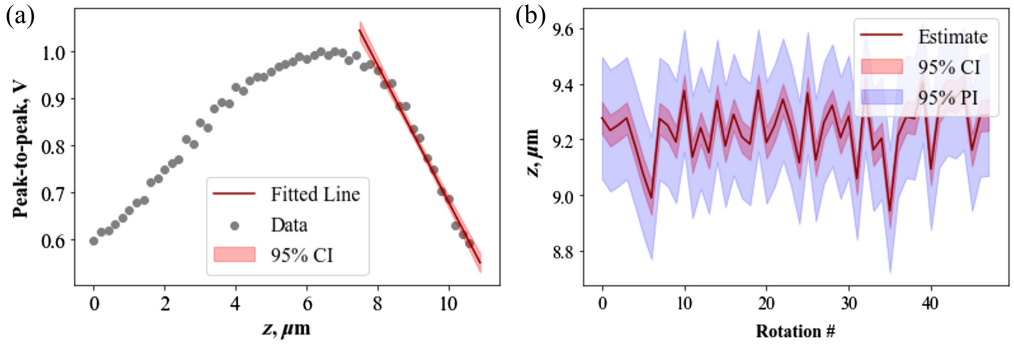

Fig. 10 (a) Depth response curve of the CFS signal. A line is fitted through the linear region of the curve (shown in red) to be used as a calibration curve to measure the axial wobble of the rotation stage. (b) Axial wobble of the rotation stage measured at 80 μm from the center of rotation. CI, confidence interval; PI, prediction interval. The sample used for measurement consists of a Si wafer with grating lines of 10 μm width fabricated on it.

5.2 Measurement Using Depth–Response Curve

To measure the axial wobble at a specific position, the CFS scan head, mounted on the piezo stage, was first positioned to a z-position in the linear range. The sample with the line structure is then scanned at a constant radius through a number of rotations. The signal peak-to-peak is retrieved and the corresponding z-position is calculated.

Figure 10(b) shows the calculated z-values for 50 rotations. During the measurements, the CFS scan head traces a circle of a constant 80 μm radius on the sample. The sample mounted on the rotation stage was rotated at a frequency of 3.16 Hz. The measured axial wobble at a point is less than 0.9 μm with a prediction interval (PI) of 95%. The prediction interval accounts for both measurement uncertainty and inherent variations in the wobble, making it more comprehensive than the confidence interval. A similar process using a sample with repeating structures can be used to measure the axial wobble during one rotation.

The axial wobble can impact the repeatability of the CFS measurements as the signal amplitude varies with the axial position. The influence is minimal when the sample is placed in the plane with the largest signal amplitude. This is evident from Fig. 10(a), where the slope is the least at the maximum. Depending again on the applications, a feedback system can be employed to ensure that the scan head is in focus throughout the scan. Another solution would be to use a lens with a longer depth of focus such that the signal peak-to-peak remains the same for a longer range of motion along the z-direction but comes at the cost of the system resolution.

6 Applications

In this section, we illustrate two possible applications of the rotation-based CFS system: particle detection on a Si wafer and calibration of etched pits with different diameters.

6.1 Particle Detection on Si Wafer

The effectiveness of the system was demonstrated by measuring PSL particles that are randomly deposited on a Si wafer. PSL particles are widely used as metrology standards to test the sensitivity of contamination detection systems. Their scattering properties also mimic those of insulating contaminants (e.g., silicon dioxide and organic residues), commonly found on wafers. Two examples are presented: Si wafers with 1 and 0.4 μm PSL particles. Figures 11(a) and 11(b) show the 2D differential scan map of the sample surface with 1 and 0.4 μm PSL particles, respectively. The scan parameters were as follows: f_{rotation}—1.1 Hz, dr—100 nm, and sampling rate—10 kS/s. The peak-to-peak of the difference signal generated from the 1 and 0.4 μm PSL particles are 0.731 ± 0.167 V and 0.256 ± 0.058 V, respectively. The values are presented with a confidence interval of 95%.

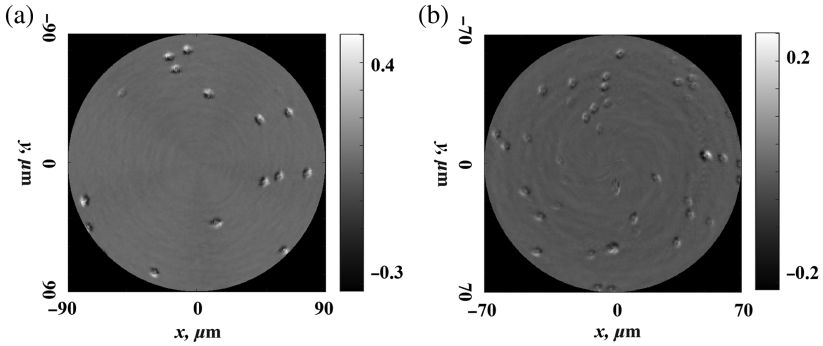

Fig. 11 2D difference map of PSL particles on Si wafer with (a) 1 μm and (b) 0.4 μm diameters. The samples are scanned with $f_{\text{rotation}} = 1.1$ Hz, and minimum radial step size, $dr = 0.1$ μm.

6.2 Calibration of Etched Pits with Different Diameters

Another application of the setup is to measure the geometrical parameters of different nanostructures. In this example, we use the CFS setup to measure and calibrate the diameters of pits etched into a silicon wafer. Etched structures are interesting targets due to their lower scattering signal compared with raised structures of similar dimensions, making precise measurement more challenging. The calibration sample consisted of an array of circular pits etched into a Si substrate, with diameters ranging uniformly from 225 to 1125 nm in 100 nm increments, spaced 10 μm apart and having a constant depth of 150 nm. The samples were fabricated using e-beam lithography followed by reactive-ion etching.

Figure 12 shows the plot with the variation in the peak-to-peak of the difference signal from the detector as a function of the pit diameter. Each data point is an average of 8 separate measurements with an errorbar of one standard deviation. The scan parameters were as follows: f_{rotation}—1 Hz, dr—100 nm, and sampling rate—10 kS/s. The plot demonstrates a monotonic increase in the peak-to-peak of the difference signal with the pit diameter. Furthermore, it can be used as a calibration curve to estimate an unknown pit diameter. In terms of signal-to-noise ratio (SNR), the etched pit with the smallest diameter of 225 nm (much smaller than the wavelength of 633 nm) exhibits an SNR of 8.97 dB, calculated using $\text{SNR} = 10\log_{10}(\frac{V_{\text{signal}}}{V_{\text{noise}}})$.

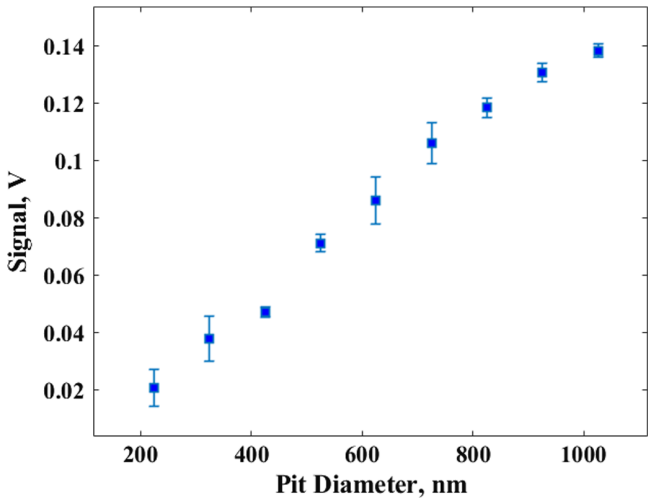

Fig. 12 Peak-to-peak of the differential signal from the split detector plotted as a function of the etched pit diameter. The pits are etched into a Si wafer with diameters varying from 225 to 1125 nm with a constant etch depth of 150 nm. Each data point is an average of 8 independent measurements.

7 Uncertainty Assessment

In this section, we detail the contributions to the measurement uncertainty from different components of the system. The maximum input voltage range of the analog-to-digital converter (ADC) is ± 10 V.

- Detector: The dark noise of the detector is measured with the detector switched on but no light incident on the bi-cell. The measured value is 0.97 mV. This includes the noise from the ADC as well.
- Laser: The laser used in the scan head is not intensity stabilized and may have fluctuations in the output power. The mean laser intensity was measured to be 1.019 W with a root mean square error of 0.006 W. The value was calculated from a 5 min measurement of the laser intensity using a power meter, 2 h after the laser is switched on. The duration of the measurement corresponds to the duration of a typical scan time. The signal varies linearly as a function of laser intensity and can differ by 0.6% from the mean value.
- Piezo: The piezo is used to step between concentric circles during the scanning. The rotational cross-talk during travel along x-axis for a maximum radius of 80 μm is 0.8 nm in z-direction. The influence of the motion error on the peak-to-peak of the signal depends on the position of the sample. Assuming the sample to be in the linear region of the calibration curve shown in Fig. 10(a), the signal can change by 0.01% of the original value.
- Rotation stage: The axial and radial wobbles from the rotation stage contribute significantly to the measurement certainty. The amount of radial wobble present in the system was not quantified, but its influence was evident from the remaining distortions in the reconstructions. The axial wobble was quantified to be less than 0.9 μm. The influence on the signal peak-to-peak again depends on the axial position of the sample following the curve, as shown in Fig. 10(a), with the signal varying between 0.31% and 11.25%.

8 Conclusion and Outlook

In this study, we introduced a rotation-based CFS system, replacing the piezo stage in the fast axis with a rotation stage while retaining a piezo stage in the slow axis for stepping across concentric circles on the sample. This setup, reminiscent of optical data storage systems, eliminates the start–stop motion characteristic of raster scans, enabling faster, continuous scanning and making it ideal for high-throughput metrology applications.

We addressed key challenges of rotational scanning such as probe centering offset and axial wobble. A frequency spread minimization approach was introduced to correct probe alignment errors without requiring reference targets. Furthermore, we estimate the axial wobble of the rotation stage to be less than 0.9 μm using the depth-dependent response of the CFS signal.

The system performance was validated through the detection of low-contrast PSL particles on silicon and the calibration of nanoscale etched pits with diameters from 225 to 1125 nm. These results demonstrate the system's potential for applications in sub-wavelength contamination monitoring and nanostructure metrology. Although the current implementation was designed as a proof-of-principle system, it demonstrates the feasibility of using rotational scanning for CFS for fast scanning. It is a compact, low-power system with a simple optical design that can be multiplexed with ease for scanning large areas.

9 Appendix A: FDTD Simulations

In this section, we detail the simulations, as shown in Fig. 2. The interaction between a sub-wavelength nanostructure and a focused spot is quite complex and needs to be modeled using a rigorous 3D Maxwell solver. These models can be used to provide a theoretical reference that can be compared with the experimental results for a better understanding of the underlying physical phenomenon behind the obtained scattered signals. For this study, we used a commercial solver (Lumerical, Ansys)[34] based on the finite-difference time-domain (FDTD) method.[35]

For the simulations, the incident field consisted of a 0.4 NA focused spot with a wavelength of 633 nm. The field is linearly polarized in the x-direction at the back focal plane of the

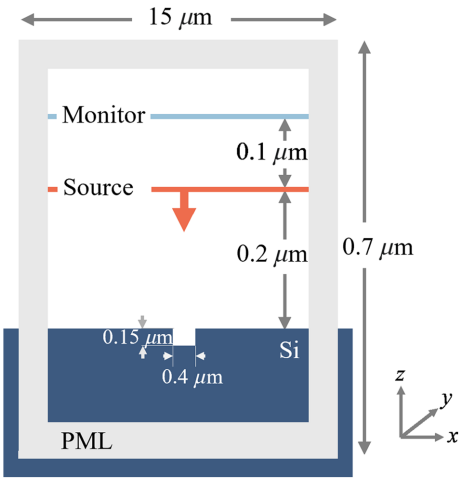

Fig. 13 Schematic of the FDTD simulation.

objective. The spot was precomputed analytically after solving the vectorial Debye integral using the formalism by Richards and Wolf[36] and was used as an imported source. Figure 13 shows the schematic of the overall simulation model. The scattering object is a pit with a diameter of 400 nm and a depth of 150 nm etched into Si (refractive index - 3.882 + i0.019). The source is injected at a height of 200 nm from the Si surface. The scattered near field is recorded using a monitor placed at a height of 300 nm from the Si surface. The complete simulation domain contains a volume of $15 \times 15 \times 0.7$ μm with perfectly matched layer boundary conditions. The far field or the field in the Fourier plane is calculated from the near field recorded using the monitor. The near-to-far-field projections are performed using built-in functions in the software.[35]

10 Appendix B: Frequency Spread Calculation: Choice of *n*

The choice of n used to calculate $S(x)$ is determined qualitatively. Low values of n result in a noisy spread—piezo position curve, whereas large values of n broaden the minima. Figures 14(a) and 14(b) plot $S(y)$ calculated using $n = 2$ and $n = 10$, respectively, for the same scan. The plot calculated using $n = 2$ is much noisier compared with the plot calculated using $n = 10$. However, the minima are much more sharper for $n = 2$ compared with $n = 10$. In both cases, the minima become hard to determine, and ultimately, the choice made is a compromise between the two.

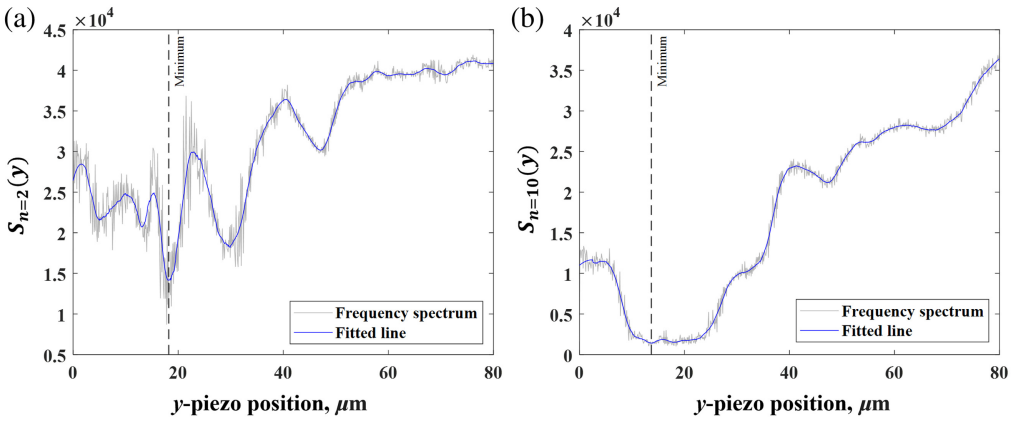

Fig. 14 Frequency spread as a function of the piezo position along the *y*-direction with the spread calculated using (a) $n = 2$ and (b) $n = 10$. Low values of n create a noisy spread–piezo position curve, whereas large values spread the minima.

Disclosures

The authors declare that there are no financial interests, commercial affiliations, or other potential conflicts of interest that could have influenced the objectivity of this research or the writing of this paper.

Code and Data Availability

The data underlying the results presented in this paper are not publicly available at this time but may be obtained from the authors upon reasonable request.

Acknowledgments

We acknowledge the Nederlandse Organisatie voor Wetenschappelijk Onderzoek (Project 17-24 Synoptics No. 2) for funding this research. We also thank Peter van der Walle from TNO for the discussion on probe centering minimization and Peter Blom from VDL for the rotation stage. We acknowledge the use of AI-assisted tools, including language and grammar checking software, to improve the clarity and readability of the paper.

References

1. A. Archenti et al., "Integrated metrology for advanced manufacturing," *CIRP Ann.* **73**(2), 639–665 (2024).
2. A. Davydov et al., "Metrology for 2D materials: a perspective review from the international roadmap for devices and systems," *Nanoscale Adv.* **6**, 2260–2269 (2024).
3. IEEE International Roadmap for Devices and Systems, "Metrology," tech. rep., Institute of Electrical and Electronics Engineers (2023).
4. N. Orji et al., "Metrology for the next generation of semiconductor devices," *Nat. Electron.* **1**, 532–547 (2018).
5. W. Häßler-Grohne et al., "Current limitations of SEM and AFM metrology for the characterization of 3D nanostructures," *Meas. Sci. Technol.* **22**, 094003 (2011).
6. A. A. Tseng, "Advancements and challenges in development of atomic force microscopy for nanofabrication," *Nano Today* **6**(5), 493–509 (2011).
7. R. B. Bergmann, M. Kalms, and C. Falldorf, "Optical in-process measurement: concepts for precise, fast and robust optical metrology for complex measurement situations," *Appl. Sci.* **11**(22), 10533 (2021).
8. M. Nouri et al., "Resolution enhancement methods in optical microscopy for dimensional optical metrology," *J. Eur. Opt. Soc.-Rapid Publ.* **21**(1), 7 (2025).
9. Y. Shimizu et al., "An insight into optical metrology in manufacturing," *Meas. Sci. Technol.* **32**(4), 042003 (2020).
10. A. C. Diebold, A. Antonelli, and N. Keller, "Perspective: optical measurement of feature dimensions and shapes by scatterometry," *APL Mater.* **6**, 058201 (2018).
11. A. Fernández Herrero et al., "Analysis of line-edge roughness using EUV scatterometry," *Nanomanuf. Metrol.* **5**, 149–158 (2022).
12. G. L. Whitworth et al., "Real-time optical dimensional metrology via diffractometry for nanofabrication," *Sci. Rep.* **10**, 5371 (2020).
13. H.-T. Huang and F. L. Terry Jr., "Spectroscopic ellipsometry and reflectometry from gratings (scatterometry) for critical dimension measurement and in situ, real-time process monitoring," *Thin Solid Films* **455–456**, 828–836 (2004).
14. S. Roy et al., "High speed low power optical detection of sub-wavelength scatterer," *Rev. Sci. Instrum.* **86**, 123111 (2015).
15. N. Kumar et al., "Reconstruction of sub-wavelength features and nano-positioning of gratings using coherent Fourier scatterometry," *Opt. Express* **22**, 24678–24688 (2014).
16. M. Menzel and S. F. Pereira, "Coherent Fourier scatterometry reveals nerve fiber crossings in the brain," *Biomed. Opt. Express* **11**, 4735–4758 (2020).
17. J. Rafighdoost, D. Kolenov, and S. F. Pereira, "Coherent Fourier scatterometry for detection of killer defects on silicon carbide samples," *IEEE Trans. Semicond. Manuf.* **37**(1), 124–128 (2024).
18. S. Roy et al., "Coherent Fourier scatterometry for detection of nanometer-sized particles on a planar substrate surface," *Opt. Express* **22**, 13250–13262 (2014).
19. S. Soman et al., "Multi-beam coherent Fourier scatterometry," *Meas. Sci. Technol.* **35**, 075905 (2024).
20. Y. R. Teo, Y. Yong, and A. J. Fleming, "A comparison of scanning methods and the vertical control implications for scanning probe microscopy," *Asian J. Control* **20**(4), 1352–1366 (2018).
21. Y. K. Yong et al., "Invited review article: high-speed flexure-guided nanopositioning: mechanical design and control issues," *Rev. Sci. Instrum.* **83**, 121101 (2012).
22. X. Du and B. Anthony, "Concentric circle scanning system for large-area and high-precision imaging," *Opt. Express* **23**, 20014–20029 (2015).

23. R. Ying et al., "Precise measurement of surface topography with microstructures based on differential confocal and spiral scanning," *Measurement* **184**, 110004 (2021).
24. A. Ulčanis and A. Vaitekonis, "Rotational scanning atomic force microscopy," *Nanotechnology* **28**(10), 10LT02 (2017).
25. J. Peek et al., *Origins and Successors of the Compact Disc: Contributions of Philips to Optical Storage*, Philips Research Book Series, Springer, Germany (2009).
26. H.-L. Du et al., "A new centering method of the measuring probe for spiral scanning-based surface profile measurement systems," *Meas. Sci. Technol.* **28**, 025006 (2016).
27. J. Huang et al., "Differential confocal measurement of microstructure surface topography based on centering error optimization and wavelet threshold denoising," *Opt. Laser Technol.* **160**, 109098 (2023).
28. Y. Cui et al., "Effects of centering error of probe tip in spiral scanning AFM for large-area measurement on measuring results," in *Int. Conf. Mech. Autom. and Control Eng.*, pp. 3024–3027 (2010).
29. M. Buhmann et al., "Investigation on probe positioning errors affecting on-machine measurements on ultra-precision turning machines," *Procedia CIRP* **101**, 242–245 (2021).
30. Y. Geng et al., "An AFM-based methodology for measuring axial and radial error motions of spindles," *Meas. Sci. Technol.* **25**, 055007 (2014).
31. W. Xu et al., "A high-precision instrument for mapping of rotational errors in rotary stages," *J. Synchrotron Radiat.* **21**, 1367–1369 (2014).
32. H. Cui et al., "Measurement and analysis of the radial motion error of aerostatic ultra-precision spindle," *Measurement* **137**, 624–635 (2019).
33. R. Bartolini, "Optical recording: high-density information storage and retrieval," *Proc. IEEE* **70**(6), 589–597 (1982).
34. Ansys Lumerical FDTD, https://www.lumerical.com/ (accessed 15-02-2025).
35. A. Taflove, S. Hagness, and M. Piket-May, *Computational Electromagnetics: The Finite-Difference Time-Domain Method*, pp. 629–670, Elsevier Inc (2005).
36. B. Richards and E. Wolf, "Electromagnetic diffraction in optical systems. II. Structure of the image field in an aplanatic system," *Proc. R. Soc. Lond. Ser. A* **253**, 358–379 (1959).

Sarika Soman is a PhD candidate in optics at the Delft University of Technology. She holds a master's degree in applied physics from the Delft University of Technology and a bachelor's degree in engineering physics from NIT, Calicut. Her research focuses on experimental optics, specifically optical metrology.

Bastiaan In 't Velt is currently pursuing a master's degree in applied physics at Delft University of Technology (TU Delft), The Netherlands. He obtained his bachelor's degree in applied physics from TU Delft in July 2024. His academic interests span a broad range of topics within the field of applied physics.

Roland Horsten is a system engineer with over 35 years at the TU Delft. An expert in analogue electronics and software, he supports research and education at the Faculty of Applied Sciences. Skilled in hardware and software integration, he designs lab equipment and custom software in C, Python, and LabVIEW. He also mentors students, contributes to optics research, and co-authors papers, earning a reputation as a versatile and valued academic collaborator.

Silvania Pereira holds the position of associate professor at the Delft University of Technology, in Delft, The Netherlands. Her recent research is in several areas related to optics, namely high numerical aperture imaging systems, photonics, optical lithography and optical metrology. She has several collaborations with national and European universities, European metrology institutes, and with the high-tech industry. She is member of the board of Photonics NL.